Mimicry of a biophysical pathway leads to diverse pollen-like surface patterns

Jiaqi Liu[a], Asja Radja[b,c], Yuchong Gao[a], Rui Yin[a], Alison Sweeney[b], and Shu Yang[a,1]

[a]Department of Materials Science and Engineering, University of Pennsylvania, Philadelphia, PA 19104; [b]Department of Physics & Astronomy, University of Pennsylvania, Philadelphia, PA 19104; and [c]School of Engineering and Applied Sciences, Harvard University, Cambridge, MA 02138

Edited by David A. Weitz, Harvard University, Cambridge, MA, and approved February 28, 2020 (received for review October 31, 2019)

A ubiquitous structural feature in biological systems is texture in extracellular matrix that gains functions when hardened, for example, cell walls, insect scales, and diatom tests. Here, we develop patterned liquid crystal elastomer (LCE) particles by recapitulating the biophysical patterning mechanism that forms pollen grain surfaces. In pollen grains, a phase separation of extracellular material into a pattern of condensed and fluid-like phases induces undulations in the underlying elastic cell membrane to form patterns on the cell surface. In this work, LCE particles with variable surface patterns were created through a phase separation of liquid crystal oligomers (LCOs) droplet coupled to homeotropic anchoring at the droplet interface, analogously to the pollen grain wall formation. Specifically, nematically ordered polydisperse LCOs and isotropic organic solvent (dichloromethane) phase-separate at the surface of oil-in-water droplets, while, different LCO chain lengths segregate to different surface curvatures simultaneously. This phase separation, which creates a distortion in the director field, is in competition with homeotropic anchoring induced by sodium dodecyl sulfate (SDS). By tuning the polymer chemistry of the system, we are able to influence this separation process and tune the types of surface patterns in these pollen-like microparticles. Our study reveals that the energetically favorable biological mechanism can be leveraged to offer simple yet versatile approaches to synthesize microparticles for mechanosensing, tissue engineering, drug delivery, energy storage, and displays.

surface patterns | pollen grains | liquid crystal elastomers | elasticity | phase separation

Surface patterns are ubiquitous in biological systems. Biological cells are topologically spherical, and many cell types, including fungal spores, pollen grains, and insect cuticles, have evolved diverse yet unique micrometer-scaled surface textures comprising spikes, stripes, and holes (1). Among them, pollen cells have some of the most ornate and elaborate surface patterns found in nature. The surface patterns of a single species are nearly identical and robust over many generations. While the biological function of pollen surface patterns has not yet been elucidated, the ability to recapitulate these hardened surface textures in synthetic systems will offer more broadly tunable functions for applications known to benefit from textured surfaces with increased surface areas, including mechanosensing (2, 3), tissue engineering (4), drug delivery (5), and energy storage (6, 7). The intricate patterns of pollen grain surfaces were recently revealed to form due to three physical conditions (8) (Fig. 1*B*): 1) An initially homogeneous material phase-separates on or near the surface of a spherical cell (*SI Appendix*, Fig. S1*A*), 2) the surface of the sphere deforms, and 3) the coupling of the phase separation to the deformed elastic layer sets the length scale of pattern features (*SI Appendix*, Fig. S1*B*). In pollen, the phase-separating material is a complex mixture of polysaccharides and some proteins that phase-separates into two distinct phases representing, for example, more and less branched polysaccharides. The deformable surface is the cell membrane, while an outer capsule, or callose wall, confines and mechanically couples the polysaccharide phase separation to the cell membrane and induces their physical contact (Fig. 1*B* and *SI Appendix*, Fig. S1). Tuning the parameters representing the underlying physicochemical composition of the cell reveals a pattern phase diagram with diverse surface textures and geometries. About 10% of extant pollen surface patterns are consistent with minima of this free energy, while the remaining 90% are patterned states consistent with arrest prior to equilibrium (8).

Given the vast chemical complexity of biological systems, realizing this rich, functional pattern space for engineering purposes will require a synthetic system that is simpler and more controllable. Despite advances in synthesis of patterned microparticles, including self-assembly of emulsions of block copolymers or polymer blends (9–11), seeded dispersion polymerization (12, 13), lithography (14), and microfluidics (15, 16), it remains rare to create robust, uniform (sub)micrometer-sized pollen-like particles with diverse but controllable surface textures, all from a single material system. Here, we experimentally recapitulate the three conditions of the biological system via physicochemical analogs and realize an analogous energetically downhill pathway of the natural pollen system within liquid crystal elastomer (LCE) microparticles (see *SI Appendix*, Table S1 for a comparison between the components of pattern formation in pollen grains and LCE microparticles). The surface patterns in both LCE particles and pollen grains form through a phase separation that is physically coupled to a competing surface process that prevents the phase separation from going to completion. While the phase separating and the competing process involve different materials in LCE particles and pollen grains, it is the presence of a physical coupling of both processes that governs patterning in these two

Significance

Biological cells, including fungal spores, pollen grains, and insect cuticles have evolved diverse micron-scaled surface patterns. Inspired by the pollen grain patterning mechanism, here, we report the synthesis of a variety of pollen-like, patterned liquid crystal elastomer (LCE) microparticles using microfluidics and reveal that an energetically downhill biological mechanism can be leveraged to offer facile methods for synthesis. Within a droplet, the short-chain liquid crystal polymers, referred to as liquid crystal oligomers (LCOs), phase-separate from an organic solvent, LCOs phase-segregate by chain lengths, and the LCO chains align perpendicularly at interface, followed by photopolymerization. All of these contribute to the formation of robust, uniform-sized pollen-like microparticles with diverse but controllable patterns from a single material system.

Author contributions: J.L., A.R., A.S., and S.Y. designed research; J.L., A.R., Y.G., and R.Y. performed research; J.L., A.R., Y.G., A.S., and S.Y. analyzed data; and J.L., A.R., A.S., and S.Y. wrote the paper.

The authors declare no competing interest.

This article is a PNAS Direct Submission.

[1]To whom correspondence may be addressed. Email: shuyang@seas.upenn.edu.

This article contains supporting information online at https://www.pnas.org/lookup/suppl/doi:10.1073/pnas.1919060117/-/DCSupplemental.

First published April 16, 2020.

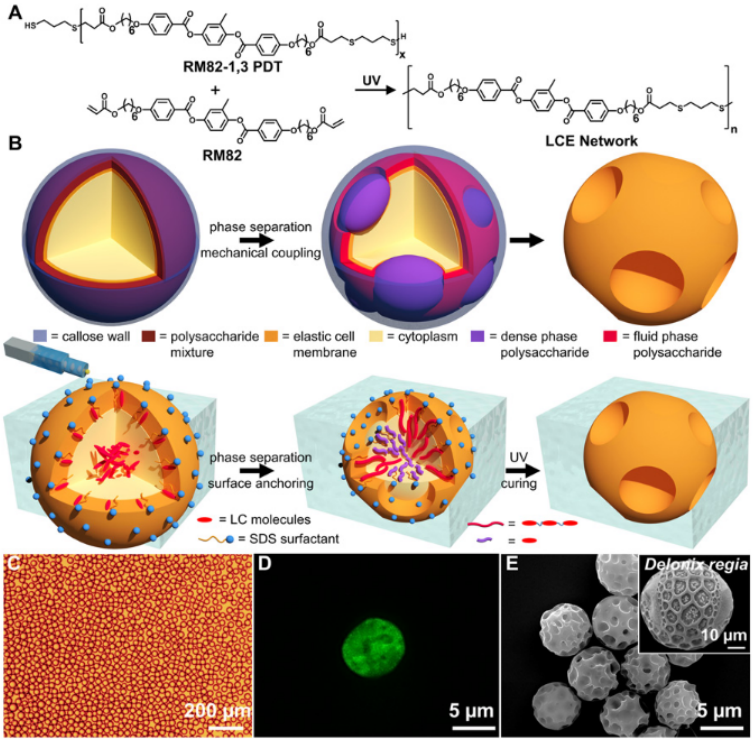

Fig. 1. Phase separation in the fabrication of spherical LCE microparticles. (*A*) Schematic illustration of the thiol-acrylate click reaction between LC monomer RM82 and LC oligomers RM82-1,3 PDT to obtain the LCE network; *x*, the number of repeat units of RM82-1,3 PDT. (*B*) Schematic illustration of surface pattern formation in natural pollen grains via the polysaccharide phase separation coupled to cell membrane undulations (*Upper*), and formation of pollen-like LCE particles, highlighting the microfluidic fabrication of LCO droplets, DCM evaporation and UV cross-linking (*Lower*). The orange shell represents the penetration length of distortions in the director field, and the yellow represents the core of the droplet that is not distorted in *Lower*. (*C*) Bright-field optical image of LCO droplets in 0.1 wt % SDS solution before DCM evaporation; droplet size is around 30 μm. (*D*) Z-stack projection confocal image of LCO droplet in 0.1 wt % SDS aqueous solution after DCM evaporation and complete phase separation. (*E*) SEM image of UV cross-linked LCE particles after exposed to UV dosage of 400 J/cm^2. (*Inset*) SEM image of pollen pattern with holes from Delonix regia. Image credit: (*Inset*) PalDat/H. Halbritter.

systems. In our LCE particles, the three conditions outlined above are realized as follows: 1) Liquid crystal oligomers (LCOs) phase-separate from an organic solvent in droplets while simultaneously segregating into short and long chains, 2) LCOs are homeotropically anchored at the surface of the droplet, and 3) the interplay and mechanical coupling between conditions 1 and 2 determine the length scale of surface patterns. It is important to emphasize that there are two phase separation processes in our LCE particle system: 1) LCO/dichloromethane (DCM) phase separation and 2) the phase segregation of long- and short-chain LCOs to regions of different curvatures. These two phase separation processes, in competition with the director field that favors homeotropic anchoring, result in surface patterns. We tune the resulting surface patterns via the surface anchoring, LCO composition, chain length heterogeneity, and rate of polymerization, among other physicochemical features.

Results and Discussion

Condition 1: Phase Separation in the Fabrication of Spherical LCE Microparticles. Particle fabrication begins with the synthesis of LCOs, consisting of thiol-terminated oligomers, RM82-1,3 propanedithiol (RM82-1,3 PDT) (Fig. 1*A*), and monomer, RM82 (1:1 molar ratio), mixed in DCM at 0.023 wt % using conventional flow-focusing capillary microfluidics (Fig. 1*B*) to form 30-μm microdroplets (Fig. 1*C*). LCO/DCM forms the oil phase, and water with poly(vinyl alcohol) (PVA) or sodium dodecyl sulfate (SDS) constitutes the outer fluid. Although we alter concentrations and conditions in later experiments, here we keep the SDS concentration around the critical micelle concentration (CMC; above which concentration the surfactant starts forming micelles) at 0.1 wt % (Fig. 1 *C*–*E*). Due to the high volatility of DCM, it diffuses out of the droplets and into the aqueous phase from which it evaporates. Furthermore, only when the DCM concentration is low enough due to this diffusion (i.e., intermediate/late stage of DCM evaporation), DCM and LCOs phase-separate, while the LCOs nematically align and organize at the droplet interface. Simultaneously, polydisperse LCO mixtures of short and long chains inside the LCO droplet phase-segregate to regions with different curvatures (see detailed discussion in *Condition 3: Interplay and Mechanical Coupling between Homeotropic Anchoring and Phase Separation*). We confirm that this phase separation can start either from inside the droplet or at the surface through confocal imaging of the intermediate stage of phase separation (*SI Appendix*, Fig. S2, arrows). After phase separation but before ultraviolet (UV) cross-linking, the droplet diameter decreases to 5 μm, and we observe holes both throughout the interior and on the surface of the droplet in confocal imaging (Fig. 1*D*) (17, 18). We further confirm that microparticles fabricated without DCM are also nematically aligned but form smooth surfaces that do not show evidence of the phase separation (*SI Appendix*, Fig. S3). In the final step of particle synthesis, we UV-crosslink droplets via

oxygen-mediated thiol-acrylate click reactions (19) (400 J/cm^2 at 20 mW·cm^{-2}) to form stable LCE particles; this step does not alter the droplet size or surface patterns. As an example, we show that LCE particles formed with 0.1 wt % SDS (Fig. 1*E*), near the CMC, have surface patterns resembling the reticulate patterns found on some pollen grain species such as *Delonix regia* (Fig. 1*E*, *Inset*). Therefore, we have developed a method of synthesizing LCE particles that mimics both the biological pathway and the final surface morphology of pollen grains.

Condition 2: Surface Anchoring of LCOs. Above, we identified that our LCE particle surfaces are deformed because of the phase separation of DCM from LCOs with an elastic contribution. Next, we discuss the role of the surface anchoring of LCOs at the interface. This surface anchoring competes with the DCM/LCO phase separation by trying to maintain the homeotropic alignment of LCOs at the interface, and thus keeps the surface from fully phase separating. Therefore, we now explore the effects of surfactant-dependent alignment of LCOs at the droplet interface on microparticle surface morphology. LCOs align perpendicularly to the surface (homeotropic anchoring) in the presence of SDS, and, tangentially, to the surface (planar anchoring) in the presence of PVA (20). Accordingly, polarized optical microscopy (POM) images of our particles show one hedgehog defect at the droplet center from 1 wt % SDS (Fig. 2 *B* and *H*), and "boojum" defects at the poles of the droplets from 1 wt % PVA (Fig. 2 *A* and *G*). The type of LCO anchoring influences the surface texture of particles via the interplay between surface anchoring energy and phase separation. In the case of planar anchoring, microparticles made with 0.5 wt %, 1 wt % PVA or 10 wt % polyvinylpyrrolidone (PVP; another surfactant that induces planar anchoring) all have smooth surfaces and are therefore not of primary interest to us in this study (*SI Appendix*, Fig. S4*B* and Fig. 2D, respectively). We hypothesize that LCO chains under planar anchoring conditions have high mobility at the interface, allowing for rearrangements of the chains that reduce the effects of the phase separation and hole formation. Microparticles made with 1 wt % SDS, instead, have surfaces patterned with divots (Fig. 2*E*). Thus, the homeotropic anchoring condition is essential for pattern formation in LCE microparticles and is analogous to the role that the cell membrane plays in the pattern formation of pollen grain surfaces. Finally, we mix 0.2 wt % SDS with 1 wt % PVA to create homeotropically aligned LCE particles with a smooth texture in the regions between holes. While the SDS induces the homeotropic anchoring and therefore a patterned surface, the presence of PVA smooths out the regions between the holes. This combination of the two surfactants indeed leads to surface patterns with well-defined holes, that is, a sharp definition between the hole and the smooth surface regions (Fig. 2 *C*, *F*, and *I*).

Condition 3: Interplay and Mechanical Coupling between Homeotropic Anchoring and Phase Separation. The absence of a competing condition would cause DCM to completely phase-separate from LCOs, forming one void in a solid sphere. However, we do not observe this morphology in our experiments; instead, all particles with homeotropic anchoring conditions are patterned with a distribution of holes on the entire surface. When we mainly focus on the late stage of phase separation, in our LCE microparticles, we hypothesize that the phase separation, which distorts the director field at the nematic–isotropic interface, competes with the perpendicular alignment of LCO chains at the interface due to homeotropic anchoring. The interplay and mechanical coupling between these two determine the length scale for patterns on the

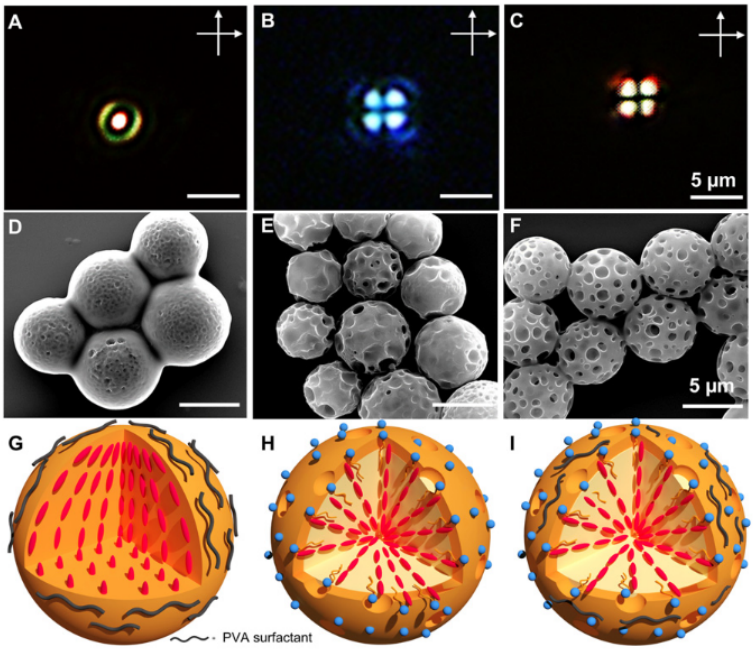

Fig. 2. Surface anchoring of LCOs. (*A–C*) POM images of LCO droplets after DCM evaporation and before UV cross-linking, illustrating surface anchoring conditions. (Scale bars, 5 μm.) (*D–F*) SEM images of LCE particles after UV cross-linking, illustrating the relationship between pattern types and surfactant anchoring conditions by changing surfactants in the aqueous phase. (Scale bars, 5 μm.) (*G–I*) Simplified illustrations of interactions between LCO chains and surfactants without showing the chain segregation effect. The black line is PVA surfactant. (*A*, *D*, and *G*) LCE particles from 1 wt % PVA. (*B*, *E*, and *H*) LCE particles from 1 wt % SDS. (*C*, *F*, and *I*) LCE particles from 1 wt % PVA with 0.2 wt % SDS.

droplets. The length scale of distortions below the surface, so-called penetration depth, is of the order $K/(2^*W)$ (21–23), where K is the average elastic constant, and W is the anchoring strength. Because the surface can deform itself to accommodate for distortions in the director field due to phase separation, the penetration depth over which this deformation is allowed decreases as the anchoring strength increases (due to higher SDS concentrations). Since the homeotropic anchoring dictates organization of LCOs at the particle surface, tuning the degree of elasticity via anchoring conditions should influence the interplay between surface energy and LCO elastic energy, and thus the pattern generated.

We then synthesize LCE microparticles with varied SDS concentrations to alter anchoring conditions. We also synthesize microparticles from monomeric constituents that lack LC order altogether, using trimethylolpropane ethoxylate triacrylate (ETPTA) as controls. As expected, at a concentration well below the CMC of SDS (0.01 wt %), ETPTA particles collapse completely (Fig. 3*A*), suggesting these droplets do not have sufficient surface energy to form stable spheres. In contrast, at the same SDS concentration (0.01 wt %), high-frequency divots form on LCE particles, suggesting that LCOs are stabilized at the interface (Fig. 3 *B* and *I*). As SDS concentration is increased to 0.05 wt % SDS, the holes transition from intercalating through the particle bulk to remaining predominantly at the particle surface (Fig. 3*C*). At the CMC (0.1 wt % SDS), the holes become shallow divots mostly restricted to the surface (Fig. 3 *D* and *J*). The extraordinary stability of LCE microparticles and surface pattern formation at concentrations below CMC confirms the importance of surface anchoring.

When SDS concentration is above CMC (0.5 wt % to 1 wt %), the holes are specifically localized to the surface (Fig. 3 *E*, *F*, and *K*). These features become less pronounced at 2 wt % SDS and nearly absent at 4 wt % as the homeotropic anchoring strength increases (Fig. 3 *G* and *H*). The interfacial tension of the droplets decreases from 34.2 mN/m below CMC (0.01 wt %) to 21.6 mN/m at the CMC (0.1 wt %); the surface elasticity also decreases (24) (see schematics in Fig. 3 *I*–*K*). Therefore, 1) coupling between the phase separation that creates distortions in the director field and anchoring conditions attempting to hinder the nematic deformation at interface, and 2) the increased interfacial stability are responsible for increasing the pattern size and decreasing the amplitude of the surface patterns with stronger anchoring conditions. Anchored LCE particles are extraordinarily stable and reproducible compared to those formed from ETPTA, which have randomly distributed holes of different sizes and shapes and do not exhibit batch-to-batch control (*SI Appendix*, Fig. S5).

We further explore the interplay between surface energy and phase transition by examining the effect of LCO chain length polydispersity. In general, mixtures of heterogeneous chain lengths tend to phase-separate (25, 26). LCOs synthesized by free-radical-mediated click reactions (27) (*SI Appendix*, Fig. S6) are, by nature, polydisperse. Typically, this is considered disadvantageous in self-assembly processes, as it generates phase instability and heterogeneity. However, in our system, polydispersity and its contribution to phase separation are fundamental components of the desired pattern formation mechanism. We characterize the molecular weight and distribution of RM82-1,3 PDT oligomers with size exclusion chromatography (SEC). Monomers are the most frequent (*SI Appendix*, Table S2). As oligomerization time increases from 1 d to 18 d, chains grow longer, the mole fraction of longer chains increases, and the fraction of shorter chains decreases (Fig. 4*H* and *SI Appendix*, Table S2 and Fig. S7). To study the effect of average chain length on phase transition properties of these mixtures, we measure their nematic-to-isotropic transition temperature (T_{NI}) and interfacial tension. As the number-average chain length $\langle l \rangle$ of RM82-1,3 PDT (averaged over the number of repeat units, x, seen in Fig. 1*A* and their mole fractions in *SI Appendix*, Table S2) increases from 2.93 to 4.00, T_{NI} increases from 41.9 °C to 48.5 °C (Fig. 4*I*), and the interfacial tension increases from 21.6 mN/m to 27.4 mN/m (*SI Appendix*, Fig. S8).

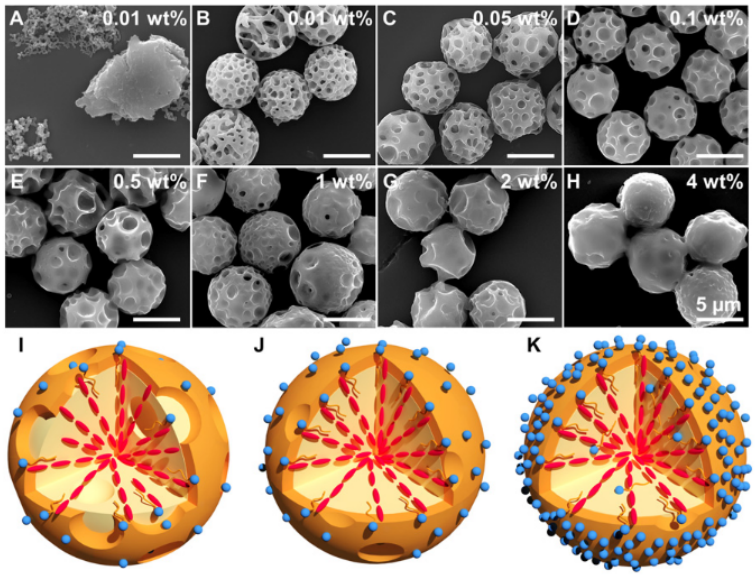

Fig. 3. Interplay and mechanical coupling between surface anchoring and phase separation by varying surfactant concentrations. (*A*) ETPTA ($M_w \approx 428$) particles from 0.01 wt % SDS (below CMC). (*B*–*H*) SEM images of LCE particles fabricated from different concentrations of SDS solutions. (Scale bars, 5 μm.) (*I*–*K*) Simplified illustrations of LCO-SDS interactions without showing the chain segregation effect (*I*) below, (*J*) around, and (*K*) above CMC of SDS aqueous solutions.

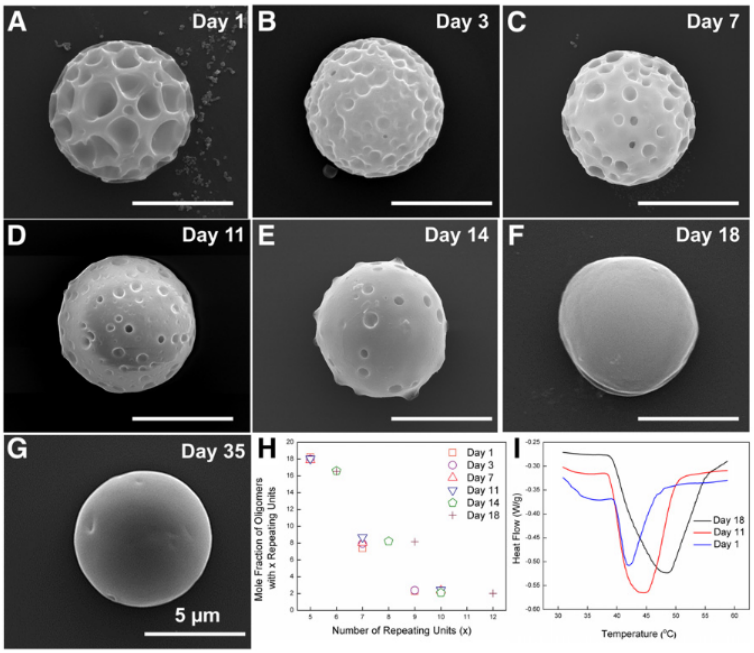

Fig. 4. The effect of LCO chain length variation on surface patterns. (*A*–*G*) SEM images showing pattern evolution on LCE particle surfaces obtained from LCO droplets dispersed in 0.1 wt % SDS aqueous solutions, which were left to sit at room temperature in the dark over an extended period of time before UV cross-linking. The scale bar in *G* applies to *A*–*F*. (*H*) Mole fraction growth of long chains and increase in the number of repeating units in each oligomer mixtures as a function of oligomerization time. Data are from SEC spectra. (*I*) DSC curves of LCOs as a function of oligomerization time. T_{NI} of LCOs increases as a function of oligomerization time.

To study the effect of $\langle l \rangle$, we fabricate LCO droplets in 0.1 wt % SDS and equilibrate them in the dark at room temperature for 35 d, during which time the chains of RM82-1,3 PDT grow slowly (27). We sample them every 2 d or 4 d for UV curing, to monitor the pattern formation. The ∼1-μm-scale divots present on LCE particle surface on day 1 nearly disappear on day 18 (Fig. 4 *A*–*F*). This is consistent with a process in which shorter chains lower the interfacial tension and aggregate in regions of larger mean curvature (28), that is, in the divots. As $\langle l \rangle$ increases, longer chains aggregate to regions of smaller mean curvature. The difference in T_{NI} serves as the thermodynamic driving force for phase segregation of different chain length LCOs (25). Presumably, shorter-chain LCOs tend to concentrate to the central hedgehog defect area with high elastic deformation (29, 30), whereas longer-chain LCOs aggregate toward the interface, flattening out the divots. On day 18, the surface becomes completely smooth and stays smooth thereafter (Fig. 4*G*). Therefore, the nature and extent of the isotropic–nematic phase transition within the particle tunes the size and maturity of divots in the final pattern. Analogously, during pollen pattern formation, the extent of the phase separation process determines the final morphology of surface patterns. Earlier arrest results in more-randomly distributed holes on the surface, while phase separation that goes to completion results in patterns with a well-defined length scale on the surface.

We then explore the formation of fingerprint-like surface patterns as seen on *Aristolochia manshuriensis* pollen (Fig. 5*A*). Cholesteric liquid crystals (CLCs) are known for their fingerprint textures on surfaces under homeotropic anchoring condition (20) (*SI Appendix*, Fig. S9). To obtain CLCs in our particles, we add a small amount of chiral dopant ((S)-4-cyano-40-(2-methylbutyl) biphenyl [CB15]) to the nematic liquid crystal (LC) host ((4-cyano-40-pentylbiphenyl) [5CB]). In this particle synthesis, we set the concentration of LCO to be 10 wt %, 5CB as 80 wt %, and CB15 as 10 wt %, inducing helices with a 5-μm pitch. The higher-than-typical CB15 concentration [10 wt % vs. 2.8 wt % (20)] is necessary, since long-chain LCOs require more energy to twist. The cholesteric LCO droplet after DCM evaporation is shown in *SI Appendix*, Fig. S10, and the resulting particles exhibit wave-like surface undulations (Fig. 5*B*).

We also create microparticles with the spike-like patterns observed in nature. While maintaining a total UV dosage of 400 J/cm^2, we alter the kinetics and nature of the LC phase separation by varying the flux from 20 mW·cm^{-2} to 85 mW·cm^{-2}. At 85 mW·cm^{-2}, the gel fraction is roughly twice that of 20 mW·cm^{-2} (*SI Appendix*, Fig. S11). We do not observe an effect of the faster cross-linking at 0.1 wt % SDS. At 0.01 wt % SDS, however, we observe a spiky surface, resembling *Ipomoea cholulensis* pollen grains (Fig. 5 *C* and *D*). We surmise that weak surface anchoring combined with shorter equilibration due to fast cross-linking results in many smaller LC domains at the surface with a spike-like morphology.

In conclusion, we recapitulate the biophysical pathway of pollen grain pattern formation to create LCE microparticles with diverse surface patterns through solvent evaporation-induced phase separation in droplets, mechanosensing and competition with the director field distortion, and a mechanical coupling between the two. Polydispersity of LCOs is a necessary feature in this process, while the tuning of the anchoring strength and LC phase transition through the average LCO chain length, composition, and cross-linking rate, and thus their preference for different surface curvatures, allow us to access the patterns found on many different natural pollen grains. It is clear that energetically favorable biological mechanisms offer simple and versatile

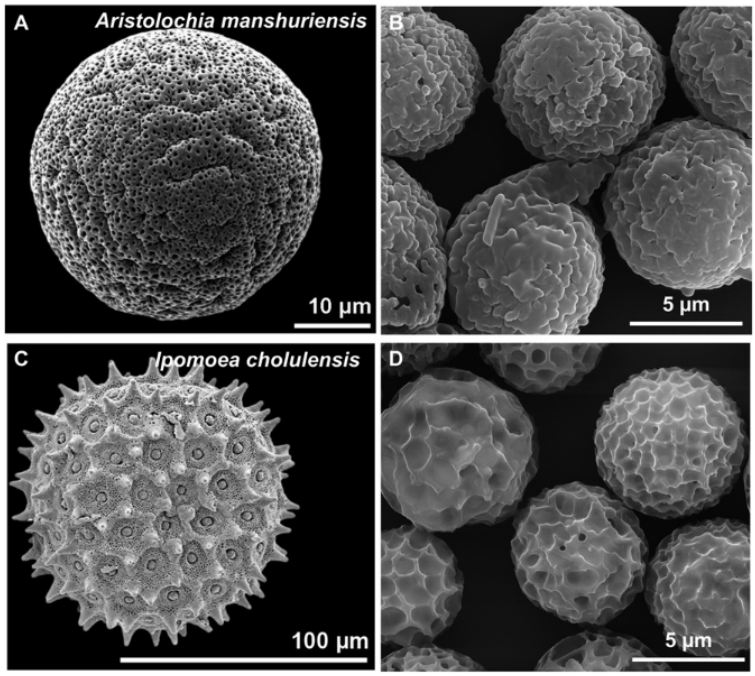

Fig. 5. The effect of cholesteric LC order and UV cross-linking rate. SEM images. (*A*) Natural pollen pattern with stripes from *A. manshuriensis*. (*B*) Pollen-like LCE particles mimicking pollen patterns with stripes from 0.1 wt % SDS using 0.3 mg/mL mixture in DCM, which contains 80 wt % nematic LC 5CB and 10 wt % chiral dopant CB15 along with 10 wt % 1:1 mol ratio of RM82 and RM82-1,3 PDT. (*C*) Natural pollen pattern with spikes from *I. cholulensis*. (*D*) Pollen-like LCE particles mimicking pollen patterns with spikes from 0.01 wt % SDS, where higher initial UV intensity at 85 mW·cm^{-2} was applied in this case. Image credit, *A* and *C*: PalDat/H. Halbritter.

approaches to engineer uniform-sized, (sub)micrometer-sized particles with diverse surface patterns in a reproducible and scalable fashion, which, in turn, will offer model systems to understand transient arrest in biological cells, and will enable applications including drug delivery, tissue engineering, energy storage, and displays.

Materials and Methods

Materials. DCM was purchased from Fisher Scientific. Photoinitiator 2,2-dimethoxy-2-phenylacetophenone (DMPA), fluorescent dye (N, N-bis(2,5-di-tert-butylphenyl)-3,4,9,10-perylene dicarboximide), surfactants PVA (Mowiol 20-98, $M_w \approx 125{,}000$), PVP ($M_w \approx 55{,}000$) and SDS were purchased from Sigma-Aldrich. Chiral dopant (S)-4′-(2-Methylbutyl)-[1,1′-biphenyl]-4-carbonitrile (CB15) was purchased from Ark Pharm. Nematic liquid crystal 4-cyano-4′-pentylbiphenyl (5CB) was purchased from Kingston Chemicals Limited. LC monomer 1,4-bis-[4-(6-acryloyloxyhexyloxy) benzoyloxy]-2-methylbenzene (RM82) was purchased from Wilshire Technologies. RM82-1,3 PDT was synthesized following the literature (19). All chemicals were used as received without further purification.

LCE Microparticle Fabrication. A glass capillary microfluidic device with flow-focusing geometry was created following the literature (31). Capillary tubes for inner fluid were purchased from Drummond Scientific Corporation (inner diameter [I.D.] 400 μm), tubes for outer fluid were from Kimble Products (I.D. 1,000 μm). The collection tubes were pulled by a PUL-1000 Micropipette Puller from World Precision Instruments. Flow rates of the aqueous and oil phases were controlled by Harvard Apparatus Pump 11 Elite. A 1:1 molar ratio of RM82 and RM82-1,3 PDT with 2 wt % photoinitiator (DMPA) were dissolved in DCM at 0.3 mg/mL (0.023 wt %) and served as oil phase. SDS or PVA at different concentrations were dissolved in deionized (DI) water and served as aqueous phase. LCO droplets were collected on either silicon wafers or glass slides and stored in aqueous solutions. The whole emulsions were kept in a homemade humidity chamber with saturation vapor pressure of water at room temperature for 24 h (although we observe that 4 h is sufficient for phase separation and formation of surface patterns) to allow DCM to completely evaporate while minimizing the evaporation of water from aqueous solutions. Then LCO droplets were exposed to UV irradiation from a four-wavelength high-power LED source operated by a DC4104 driver from Thorlabs at a total dosage of 400 J/cm^2 to ensure complete cross-linking of the LCE networks.

Characterization. Bright-field (BF) images to characterize sizes and POM images to characterize anchoring conditions of LCO droplets were taken by an Olympus BX61 Motorized Microscope with crossed polarizers. The confocal laser scanning microscopy (CLSM) z-stack projection images were taken by Leica TCS SP8 Confocal Laser-Scanning Microscope, and 0.01 wt % fluorescent dye (N, *N*-bis(2,5-di-tert-butylphenyl)-3,4,9,10-perylene dicarboximide) was added. The fluorescent dye was excited by 3.0012% 488-nm excitation laser, collected through a 77.2-μm pinhole and 580-nm emission wavelength for pinhole airy calculation, and detected by a photomultiplier tube (497 nm to 572 nm). Samples were collected on uncoated 35-mm dish with no. 1.5 coverslip and 14-mm-diameter glass from MatTek Corporation. For samples after complete phase separation, they were covered with Fluoroshield histology mounting medium from Sigma-Aldrich. For samples at the intermediate stage of phase separation, no mounting medium was used. Surface patterns of LCE particles were characterized by an FEI Quanta 600 environmental scanning electron microscope at 15-kV electron beam. Chain lengths of RM82-1,3 PDT were characterized by an EcoSEC HLC-8230 GPC size exclusion chromatography from Tosoh Corporation with THF as the eluent solvent. The differential scanning calorimetry (DSC) curves were measured by a TA Instruments Q2000 using TZero pans and lids. Samples of LCOs were heated and cooled from −10 °C to 180 °C at a ramping rate of 10 °C/min. The data from the first heating cycle were used. The interfacial tension of LCOs in 0.1 wt % SDS solution was measured by the pendant drop mode from a ramè-hart Goniometer with a 0.71-mm-outer-diameter needle. Each test was repeated three times, and the average value was reported.

Data and materials availability. All data needed to support the conclusions are presented in the main text or *SI Appendix*.

ACKNOWLEDGMENTS. We acknowledge support by NSF through the University of Pennsylvania Materials Research Science and Engineering Center (Grant DMR-1720530), and NSF/INSPIRE Grant IOS-1343159. A.R. was supported by a David and Lucile Packard Foundation Fellowship to A.S., and in part by the Schmidt Science Fellowship (https://schmidtsciencefellows.org/). We thank Lisa Tran, Randall Kamien, Maxim O. Lavrentovich, and Shenglong Shang for helpful discussion. We also thank Jasmine Zhao and Andrea Stout for assistance with confocal microscopy characterization.

1. M. O. Lavrentovich, E. M. Horsley, A. Radja, A. M. Sweeney, R. D. Kamien, First-order patterning transitions on a sphere as a route to cell morphology. *Proc. Natl. Acad. Sci. U.S.A.* **113**, 5189–5194 (2016).
2. O. Hamant, E. S. Haswell, Life behind the wall: Sensing mechanical cues in plants. *BMC Biol.* **15**, 59 (2017).
3. E. S. Hamilton *et al.*, Mechanosensitive channel MSL8 regulates osmotic forces during pollen hydration and germination. *Science* **350**, 438–441 (2015).
4. Y. Yan *et al.*, Differential roles of the protein corona in the cellular uptake of nanoporous polymer particles by monocyte and macrophage cell lines. *ACS Nano* **7**, 10960–10970 (2013).
5. H.-K. Na *et al.*, Efficient functional delivery of siRNA using mesoporous silica nanoparticles with ultralarge pores. *Small* **8**, 1752–1761 (2012).
6. Z. Chen *et al.*, High-performance supercapacitors based on hierarchically porous graphite particles. *Adv. Energy Mater.* **1**, 551–556 (2011).
7. D. Chen *et al.*, Reversible lithium-ion storage in silver-treated nanoscale hollow porous silicon particles. *Angew. Chem. Int. Ed. Engl.* **51**, 2409–2413 (2012).
8. A. Radja, E. M. Horsley, M. O. Lavrentovich, A. M. Sweeney, Pollen cell wall patterns form from modulated phases. *Cell* **176**, 856–868.e10 (2019).
9. S.-J. Jeon, G.-R. Yi, S.-M. Yang, Cooperative assembly of block copolymers with deformable interfaces: Toward nanostructured particles. *Adv. Mater.* **20**, 4103–4108 (2008).
10. T. Higuchi, A. Tajima, K. Motoyoshi, H. Yabu, M. Shimomura, Frustrated phases of block copolymers in nanoparticles. *Angew. Chem. Int. Ed. Engl.* **47**, 8044–8046 (2008).
11. H. Yabu, T. Higuchi, M. Shimomura, Unique phase-separation structures of block-copolymer nanoparticles. *Adv. Mater.* **17**, 2062–2065 (2005).
12. S. Shi *et al.*, Preparation of raspberry-like poly(methyl methacrylate) particles by seeded dispersion polymerization. *J. Appl. Polym. Sci.* **120**, 501–508 (2011).
13. S.-H. Kim *et al.*, Synthesis and assembly of colloidal particles with sticky dimples. *J. Am. Chem. Soc.* **134**, 16115–16118 (2012).
14. L. Wang, L. Xia, G. Li, S. Ravaine, X. S. Zhao, Patterning the surface of colloidal microspheres and fabrication of nonspherical particles. *Angew. Chem. Int. Ed. Engl.* **47**, 4725–4728 (2008).
15. J. Wan, A. Bick, M. Sullivan, H. A. Stone, Controllable microfluidic production of microbubbles in water-in-oil emulsions and the formation of porous microparticles. *Adv. Mater.* **20**, 3314–3318 (2008).
16. S. Xu *et al.*, Generation of monodisperse particles by using microfluidics: Control over size, shape, and composition. *Angew. Chem. Int. Ed. Engl.* **44**, 724–728 (2005).
17. I. D. Rosca, F. Watari, M. Uo, Microparticle formation and its mechanism in single and double emulsion solvent evaporation. *J. Control. Release* **99**, 271–280 (2004).
18. S. Hyuk Im, U. Jeong, Y. Xia, Polymer hollow particles with controllable holes in their surfaces. *Nat. Mater.* **4**, 671–675 (2005).
19. Y. Xia, X. Zhang, S. Yang, Instant locking of molecular ordering in liquid crystal elastomers by oxygen-mediated thiol-acrylate click reactions. *Angew. Chem. Int. Ed. Engl.* **57**, 5665–5668 (2018).
20. L. Tran *et al.*, Change in stripes for cholesteric shells via anchoring in moderation. *Phys. Rev. X* **7**, 041029 (2017).
21. V. Vitek, M. Kléman, Surface disclinations in nematic liquid crystals. *J. Phys. France* **36**, 59–67 (1975).
22. R. B. Meyer, The interaction between a disclination in a nematic liquid crystal and a rubbed surface. *Solid State Commun.* **12**, 585–588 (1973).
23. S. Faetti, V. Palleschi, Experimental investigation of surface deformations at the nematic-isotropic interface : A new method to measure the Nehring-Saupe elastic constant K13. *J. Phys. France* **46**, 415–424 (1985).
24. B. Jerome, Surface effects and anchoring in liquid crystals. *Rep. Prog. Phys.* **54**, 391–451 (1991).
25. F. Elias, S. M. Clarke, R. Peck, E. M. Terentjev, Nematic order drives phase separation in polydisperse liquid crystalline polymers. *Macromolecules* **33**, 2060–2068 (2000).
26. M. Muthukumar, C. K. Ober, E. L. Thomas, Competing interactions and levels of ordering in self-organizing polymeric materials. *Science* **277**, 1225–1232 (1997).
27. C. E. Hoyle, A. B. Lowe, C. N. Bowman, Thiol-click chemistry: A multifaceted toolbox for small molecule and polymer synthesis. *Chem. Soc. Rev.* **39**, 1355–1387 (2010).
28. H. Ibach, Ed., "Equilibrium thermodynamics" in *Physics of Surfaces and Interfaces* (Springer, Berlin, Germany, 2006), pp. 149–205.
29. B. Wagner, R. Tharmann, I. Haase, M. Fischer, A. R. Bausch, Cytoskeletal polymer networks: The molecular structure of cross-linkers determines macroscopic properties. *Proc. Natl. Acad. Sci. U.S.A.* **103**, 13974–13978 (2006).
30. I. Muševič, M. Škarabot, U. Tkalec, M. Ravnik, S. Žumer, Two-dimensional nematic colloidal crystals self-assembled by topological defects. *Science* **313**, 954–958 (2006).
31. A. S. Utada *et al.*, Dripping, jetting, drops, and wetting: The magic of microfluidics. *MRS Bull.* **32**, 702–708 (2007).